RSC Advances

PAPER

View Article Online
View Journal | View Issue

Cite this: *RSC Adv.*, 2019, **9**, 20612

Hyperbranched Co_2P nanocrystals with 3D morphology for hydrogen generation in both alkaline and acidic media

Xiaoyang Wang,[ab] Xiaomin Tian,[ab] Xiao Duan,[ab] Chun Wu,[c] Wenli Pei,*[d] Kai Wang,[a] Shuang Yuan[b] and Qiang Wang *[a]

Received 7th April 2019
Accepted 21st May 2019

DOI: 10.1039/c9ra02605c

rsc.li/rsc-advances

Hyperbranched Co_2P nanocrystals with three-dimensional structure have successfully been synthesized by a facile one-step wet-chemical method. The hyperbranched Co_2P are consisted of a large number of nanofilaments. The crystal splitting should be responsible for the formation of this structure. Catalytic performances measurements toward hydrogen evolution reaction for the obtained hyperbranched Co_2P nanocrystals demonstrate a small overpotential of 100 mV at current density of 10 mA cm^{-2}, with a Tafel slope of 67 mV dec^{-1} in 1 M KOH. Durability tests show that slight catalytic activity fading occurs after 2000 CV cycles or 22 h chronoamperometric testing. In addition, the hyperbranched Co_2P also perform well in 0.5 M H_2SO_4 with a low overpotential of 107 mV at 10 mA cm^{-2} and a Tafel slope of 69 mV dec^{-1}. This facile method provides a strategy for the preparation of low-cost metal phosphide electrocatalysts for hydrogen evolution in both alkaline and acidic media.

Introduction

The hydrogen evolution reaction (HER) has been widely studied as an important process in the electrolysis of water for hydrogen production. Due to the activation energy barrier, extra electricity is needed to overcome the overpotential. To accelerate the HER process and reduce energy loss, efficiency catalysts are highly required. Platinum and its alloys are considered to be the best HER catalysts, however, high cost and low reserves limit their widespread applications. Therefore, it is urgent to develop efficient non-precious metal HER catalysts with low cost and earth-abundance.

Recently, transition metal phosphides (TMPs) have attracted extensive attention as non-precious metal HER catalyst.[1–6] In 2005, Liu and Rodriguez found that the Ni_2P (001) possesses comparable HER activity to [NiFe] hydrogenase base on density functional theory (DFT) calculations.[7] Then the first experimental on nanoscale TMPs for HER catalysts was report by Zhang in 2013.[8] After that, great progresses have been made in HER mechanism of TMPs, and many TMPs have been developed, such as Ni_2P[9] and CoP[10] nanosheets, hollowed Co_2P, CoP and Ni_2P nanoparticles,[11–13] CoP_2/RGO[14] and CoP–CNT[15] composite structures, Co_2P and CoP nanowires,[16–18] FeP nanorods,[19] MoP nanoparticles.[20] In-depth research on the catalytic mechanism of CoP nanoparticles found that phosphorus atoms play a key role in the HER process.[11,21,22] The P atom on the surface of the transition metal phosphide with more electronegativity can act as Lewis base to trap protons and make their discharge easier, promoting the HER process.[5] In fact, most non-precious metal HER catalysts can only perform well in acidic media but not in alkaline media.[3,5] However, most oxygen evolution reaction (OER) catalysts work well only in neutral or alkaline media,[23–25] which is not match to the HER catalysts. So, it is great important to develop HER catalysts that can work well in a wide pH range to cooperate with the OER catalysts and achieve the overall water splitting. The corrosion resistance must be taken into account to achieve this purpose. Compared to metals, metal oxides and metal hydroxides, metal phosphides have better corrosion resistance.[3] Recently reported Ni_5P_4 nanocrystalline,[26] Co_2P@NPG[27] and Mn doped CoP nanosheets[28] can work well in both acid and alkali solutions. The highly corrosion resistance of TMPs provides the possibility to achieve overall water splitting.

To further enhance the HER catalytic activity and stability of TMPs, a feasible strategy is to optimize the shape of catalysts. Such as FeP hollow nanoparticles[29] exhibited a high HER activity in both acidic and neutral-pH aqueous solutions, Co_2P nanorods[30] performed well in acidic media toward HER. What's more, TMPs nanomaterials with three-dimensional (3D) structures possesses a large specific surface area similar to that of

[a]Key Laboratory of Electromagnetic Processing of Materials (Ministry of Education), Northeastern University, P. O. Box 314, No. 11, Lane 3, Wenhua Road, Heping District, 110819, Shenyang, China. E-mail: wangq@mail.neu.edu.cn

[b]School of Metallurgy, Northeastern University, P. O. Box 314, No. 11, Lane 3, Wenhua Road, Heping District, 110819, Shenyang, China

[c]School of Materials Science and Engineering, Liaoning Technical University, Fuxin 123000, China

[d]Key Laboratory of Anisotropy and Texture of Materials (Ministry of Education), Northeastern University, P. O. Box 314, No. 11, Lane 3, Wenhua Road, Heping District, 110819, Shenyang, China

low-dimensional nanomaterials, and also have a stable structure, having an important application for the HER catalysis.[31–33] For instance, urchin-like CoP nanocrystals with 3D structure reported by Yang[32] showed high activity and superior stability toward HER in acidic media. However, there are still few reports on TMPs nanocrystals with 3D structures as high-efficiency HER catalysts in a wide pH range. In this work, we report hyperbranched Co_2P nanocrystals (HB-Co_2P NCs) with 3D morphology prepared *via* a facile one-step wet-chemical method. The obtained HB-Co_2P NCs were evaluated as HER electrocatalysts. It's expected this type of particles present good performances in both alkaline and acidic media.

Experimental

Materials

The reagents used in the experiment are as follows: cobalt chloride hexahydrate ($CoCl_2 \cdot 6H_2O$, analytical grade, SCR), oleylamine (OY, C18-content 90%, Aladdin), tri-*n*-octylphosphine oxide (TOPO, 99%, J&K), tri-*n*-octylphosphine (TOP, 97%, STREM), sulfuric acid (H_2SO_4, 98%, SCR), potassium hydroxide (KOH, 95%, Aladdin) and Nafion (5%, HESEN). All materials were used without further purification.

Synthesis of hyperbranched Co_2P nanocrystals

The HB-Co_2P nanocrystals have been successfully synthesized by a modified wet-chemical method, in which a stable cobalt precursor, cobalt chloride hexahydrate was used. In a typical preparation route, $CoCl_2 \cdot 6H_2O$ (0.1189 g, 0.5 mmol) and TOPO (0.1933 g, 0.5 mmol) were mixed with oleylamine (20 mL) in a three-neck and round-bottom flask. The flask was heated to 120 °C for 1.5 h under Ar gas flow. For degassing, the reaction system was stirred by using a magnetic rotor. Then the magnetic rotor was removed out and TOP (4 mL) was injected into the flask. Another 4 mL of TOP was added after the solution was heated to 320 °C during 30 min. After the mixture was aged at 320 °C for 30 min, the flask was removed out from the heater and cooled to room temperature. The product was isolated and washed by repeated centrifugation with a small amount of hexanes and excess ethanol. Finally, part of the product dispersed in hexane and the rest was dried at room temperature into powder.

Characterizations

The morphology of the HB-Co_2P nanocrystals was characterized by transmission electron microscopy (TEM, 200 kV, JEM-2100F, JEOL) and scanning electron microscopy (SEM, SU8000, HITACHI). Powder X-ray diffraction (XRD) patterns of the powder were collected using a Rigaku SmartLab diffractometer equipped with a Cu Kα X-ray source. The chemical composition and elemental valence states were characterized by X-ray photoelectron spectroscopy (XPS, ESCALAB250).

Electrochemical performances

All electrochemical measurements were carried out with an electrochemical workstation (VSP, Bio-Logic) in a three-electrode system. 1 M KOH and 0.5 M H_2SO_4 aqueous solutions were employed as electrolyte. Ag/AgCl electrode (3 M KCl) and a platinum wire were used as the reference and counter electrode, respectively. Preparation of working electrodes is as following: 10 mg of sample powder was dispersed in 0.5 mL of ethanol along with 25 μL of Nafion solution, and the mixture was sonicated for 60 min. Then, 10 μL of the mixture was dropped onto a glassy carbon (GC) disk electrode (5 mm in diameter) to obtained a mass loading of 1 mg cm^{-2}. The 20% Pt/C modified electrode with the same loading was prepared using the same method. Cyclic voltammetry (CV) test was carried out first between −0.9 to −1.4 V *vs.* Ag/AgCl in 1 M KOH (or −0.1 to −0.6 V *vs.* Ag/AgCl in 0.5 M H_2SO_4) at a potential sweep rate of 50 mV s^{-1} for 30 cycles to obtain a stable current. Then, linear sweep voltammetry (LSV) measurements were conducted in 1 M KOH (or 0.5 M H_2SO_4) with a scan rate of 5 mV s^{-1} to obtain the polarization curves. All polarization curves were *iR*-corrected. The long-term stability tests were performed in 1 M KOH by potential cycling between −0.9 to −1.4 V *vs.* Ag/AgCl at a sweep rate of 100 mV s^{-1} for 2000 cycles. In all measurements, the Ag/AgCl reference electrode was calibrated with respect to a reversible hydrogen electrode (RHE): $E(\text{RHE}) = E(\text{Ag/AgCl}) + (0.197 + 0.059\ \text{pH})$. During the test, the electrolyte was stirred using a magnetic rotor to remove bubbles adsorbed on the surface of the electrode, and agitate the solution.

Results and discussion

The HB-Co_2P NCs were first characterized by XRD. As shown in Fig. 1a, the major diffraction peaks at 40.7°, 43.3°, 52.0° and 56.2°can be indexed to the diffraction from (112), (211), (020) and (302) planes of orthorhombic Co_2P (PDF 89-3030, $a = 5.646$ Å, $b = 3.513$ Å, $c = 6.608$ Å), respectively. Such cobalt-rich phosphide generally has an excellent conductivity similar to pure metal cobalt, which is beneficial for the HER processes.[5] The chemical composition and chemical states of Co and P in the as-prepared HB-Co_2P NCs were investigated by X-ray photoelectron spectroscopy (XPS). The XPS survey spectrum of

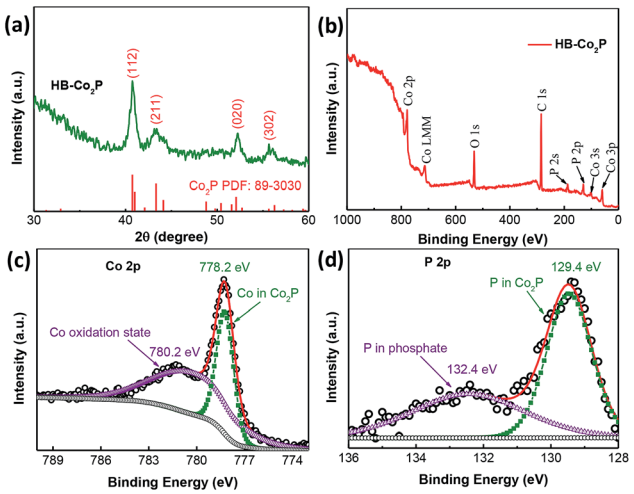

Fig. 1 (a) Experimental XRD pattern of the HB-Co_2PNCs. XPS survey spectra for the (b) HB-Co_2P NCs, (c) Co 2p and (d) P 2p regions.

the HB-Co_2P NCs as shown in Fig. 1b indicates the presence of the elements Co and P. As depicted in Fig. 1c, the high resolution scan of the Co 2p yielded two peaks at the binding energy of 778.2 and 780.2 eV. The peak at 778.2 eV is assigned to a reduced Co $2p_{3/2}$ species in Co_2P.[30] The peak at higher binding energy of 780.2 eV can be attributed to a Co oxidation state in cobalt phosphate formed on the surface of the HB-Co_2P NCs.[34] For the high-resolution XPS spectrum of P (see Fig. 1d), the observed peaks located at 129.4 and 132.4 eV. The peak at 129.4 eV corresponds to P $2p_{3/2}$, which is associated with the typical binding energy for P 2p in Co_2P.[30] Another peak at higher binding energy of 132.4 eV can be assigned to oxidized phosphate species.[34–36]

The peak at 778.2 eV for Co $2p_{3/2}$, which is positively shifted relatives to metallic Co (777.9 eV). Whereas the peak at 129.4 eV for P $2p_{3/2}$ belong to elemental P (130.0 eV) is negatively shifted. These results indicate that Co is positively charged (δ^+) and P is negatively charged (δ^-) in the HB-Co_2P NCs.[36] This charge shift may have an effect on the electrochemical performance, which is highly associated with the electronic structure.[37,38]

SEM and TEM images reveal that the overall length of the HB-Co_2P NCs is 500–900 nm, and the diameter of each individual nanofilament is ~6 nm. A typical SEM image (see Fig. 2a) demonstrates a 3D morphology of HB-Co_2P NCs. TEM images of HB-Co_2P NCs are presented in Fig. 2b–d. It can be seen that each particle was made up by large number of individual nanofilaments (see Fig. 2d). Similar structures have been reported in Bi_2S_3 [39] and Fe_2P[40] systems. These kinds of structures are considered to be hyperbranched structures due to the crystal splitting. Generally, the splitting is associated with fast crystal growth.[39] More in-depth, Zhang found that there are many kink sites in the individual nanofilaments of the hyperbranched structures, and the splitting was found to occur around the kink sites,[41] which mean that there is high density of crystal defects in the hyperbranched structures. In Fig. 2c, various forms of hyperbranched particles can be observed, such as the sheaflike (I, II), dumbbell (III) and spherical (IV) particles. The different forms of particles reflect varying degrees of crystal splitting, and the spherical particles may be the final form of splitting. High-resolution transmission electron microscopy (HRTEM) image of the nanofilament of sheaflike particle shown in Fig. 2e, which shows clear lattice fringes with lattice spacing of 0.181 nm, indexing to the (301) plane of orthorhombic Co_2P, indicating the nanofilaments grow along [301] direction.

Fig. 2f–h show the scanning TEM (STEM) images and EDX elemental mapping images of Co and P for the HB-Co_2P NCs, confirming the homogeneously distribution of the all elements in whole particles. The corresponding energy-dispersive X-ray spectroscopy (EDS) confirms the atomic ratio of Co : P close to 2 : 1.

To understand the growth process of the HB-Co_2P NCs, 2 mL of reaction solution were taken out from the three-necked flask at different holding time, and then rapidly injected into ethanol during the reaction process. The products obtained after centrifugation were dispersed in hexane for TEM detection. Fig. 3 shows the TEM images of the HB-Co_2P NCs at different stages of growth. The shape evolution of the particles can be clearly seen. Nanorods with a rough surface have been formed when the temperature rose to 320 °C without any holding time, and the particles have not yet split (see Fig. 3a). The rough surface of the nanorods ends indicates that there are many defects, which may promote the splitting of the crystal. Then, slight crystal splitting occurred at both ends of the nanorods at the holding time of 1 min (see Fig. 3b). Afterwards, the degree of crystal splitting of nanorods gradually increased, and by the time of aging for 7 minutes, individual nanofilaments could be clearly observed, and the particles show a scarf-like morphology (see Fig. 3e). Then, the length of the individual nanofilaments and the overall size of the particles gradually increased (see Fig. 3e–h) with extending the holding time. According to the

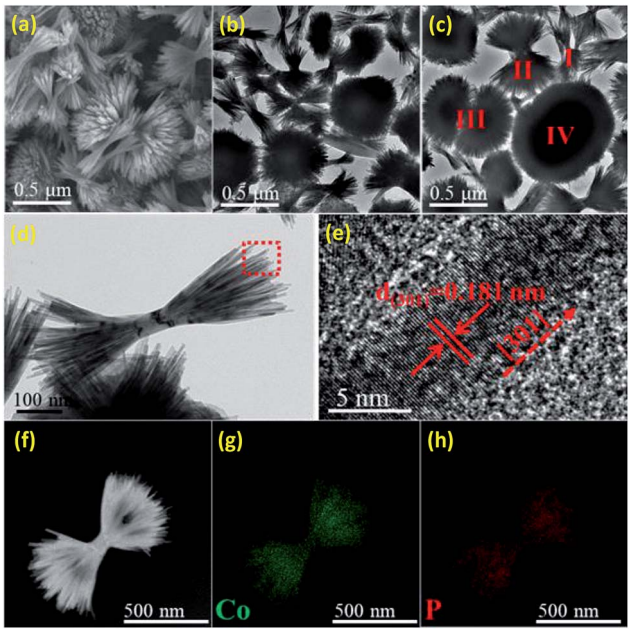

Fig. 2 (a) SEM image and (b–d) TEM images of the HB-Co_2P NCs, (e) HRTEM image for the individual nanofilament of the HB-Co_2P particle shown in (d), (f) STEM image and (g and h) EDX elemental mapping of Co, P for the HB-Co_2P NCs.

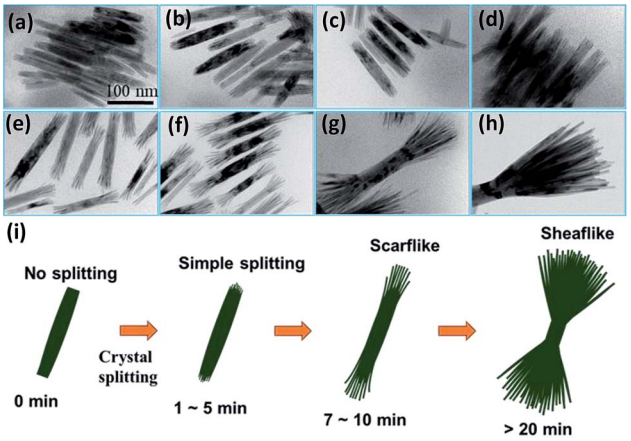

Fig. 3 TEM images of the HB-Co_2P NCs at different holding time at 320 °C: (a) 0 min, (b) 1 min, (c) 3 min, (d) 5 min, (e) 7 min, (f) 10 min, (g) 20 min, (h) 30 min. (i) Schematic of the structural evolution of the HB-Co_2P NCs. All scale bars are the same as in (a).

results, we believe that crystal splitting has already occurred at the initial stage of heat preservation. In the subsequent holding time, only the aging of the particles and the degree of crystal splitting increased. Schematic of the structural evolution is shown in Fig. 3i, which clearly describes the growth process of the HB-Co_2P NCs.

The HER performances of the as-synthesized HB-Co_2P NCs were examined in a typical three-electrode setup with a scan rate of 5 mV s^{-1}. Fig. 4 shows the HER electrocatalytic activity of the HB-Co_2P NCs and 20% Pt/C with same mass loading of 1 mg cm^{-2}. Fig. 4a presents the polarization curves obtained in 1 M KOH, it can be seen that the HB-Co_2P NCs exhibit excellent HER activity and demonstrate a low overpotential of ~100 mV at a current density of 10 mA cm^{-2} and ~121 mV for 20 mA cm^{-2}, which is superior or comparable to most of recently reported TMPs toward HER in alkaline electrolyte (see Table 1). Furthermore, in the larger current density region, the overpotential required for the HB-Co_2P NCs is similar to 20% Pt/C. To obtain a current density of 100 mA cm^{-2}, overpotential of 185 and 156 mV was needed for the HB-Co_2P NCs and 20% Pt/C, respectively. Such comparisons further demonstrate the excellent catalytic activity of the HB-Co_2P NCs in alkaline media. Fig. 4b shows the Tafel curves obtained by replot the polarization curves in Fig. 4a, which give a Tafel slope of 67 and 49 mV dec^{-1} for the HB-Co_2P NCs and 20% Pt/C, respectively. The similar Tafel slopes indicate similar reaction kinetics on HB-Co_2P NCs and 20% Pt/C in alkaline media.

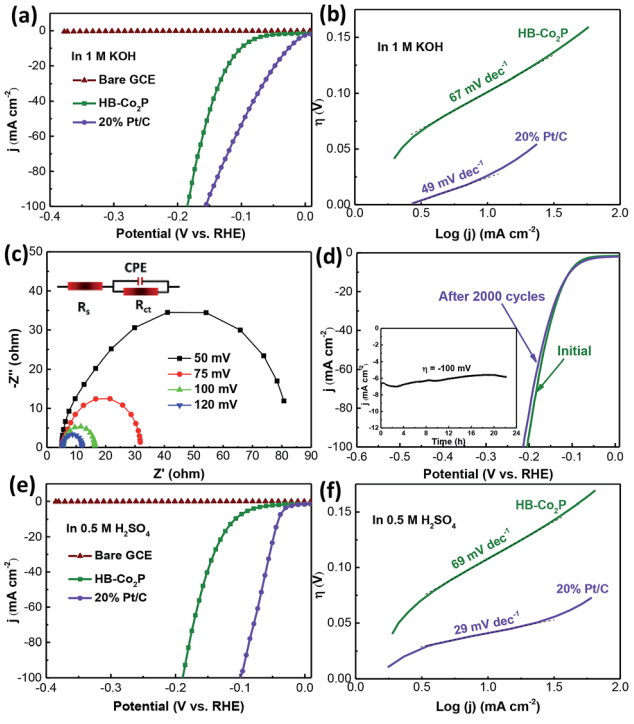

Fig. 4 (a) Polarization curves of 20% Pt/C, the HB-Co_2P NCs and bare GCE in 1 M KOH solution, (b) corresponding Tafel plots derived from (a), (c) Nyquist plots of the HB-Co_2P NCs at various HER overpotentials, inset (c) is the equivalent circuit, (d) Polarization curves before and after 2000 CV cycles of the HB-Co_2P NCs, inset (d) is chronoamperometric testing at a constant overpotential of 100 mV of the HB-Co_2P NCs. (e) Polarization curves of 20% Pt/C, the HB-Co_2P NCs and bare GCE in 0.5 M H_2SO_4 solution, (f) corresponding Tafel plots derived from (e).

As well known, hydrogen evolution reaction is a multi-step electrochemical process. In alkaline media, the first step is the dissociation of water: $H_2O + e^- \rightarrow H_{ads} + OH^-$ (Volmer reaction, 118 mV dec^{-1}), followed by electrochemical Heyrovsky step: $H_2O + e^- + H_{ads} \rightarrow H_2 + OH^-$ (Heyrovsky reaction, 39 mV dec^{-1}), or a recombination step: $H_{ads} + H_{ads} \rightarrow H_2$ (Tafel reaction, 29 mV dec^{-1}). The Tafel slope of the HB-Co_2P NCs falls in the range of 39–118 mV dec^{-1}, indicating that it follows the Volmer–Heyrovsky process. Typically, the Volmer–Heyrovsky process involves the electrochemical reduction of H_2O into adsorbed H_{ads} and OH^-, followed by the detachment of OH^- to refresh the surface and formation of adsorbed H intermediates to yield H_2.[51] As mentioned, there is a transfer of electrons density from Co to P in Co_2P, which results in Co and P are positively charged and negatively charged, respectively.[28,30] In HER process, both Co and P can be active sites. Co centers act as hydride acceptor and P centers act as proton receptor, promoting the hydrogen evolution.[35]

The electrocatalytic activity of the HB-Co_2P NCs was further examined by electrochemical impedance spectroscopy technology (EIS). Fig. 4c shows the Nyquist plots of the HB-Co_2P NCs modified electrode at various overpotentials from 50 to 120 mV *vs.* RHE. The equivalent circuit to fit the EIS data is inserted in the Fig. 4c. In which, R_s is the solution resistance, CPE and R_{ct} are the constant phase element and charge transfer resistance at HB-Co_2P/electrolyte interface, respectively. Obviously, the charge-transfer resistance (R_{ct}) decrease rapidly with increasing overpotentials from ~67 Ω at 50 mV to ~7 Ω at 120 mV. The lower resistance may be contributed by the cobalt-rich phase, indicating a faster HER kinetics at higher overpotentials, which is highly consistent with the polarization curve of the HB-Co_2P NCs in Fig. 4a.

Stability of the HB-Co_2P NCs was evaluated by CV sweeps between −0.377 and 0.123 V *vs.* RHE in the 1 M KOH solution. As depicted in Fig. 4d, there was slight decreasing on catalytic activity after 2000 CV cycles. The inset of Fig. 4d shows the chronoamperometric curve obtained at a constant overpotential of 100 mV in 1 M KOH solution. After 22 h chronoamperometric testing, slight catalytic activity fading was occurred, suggesting the superior stability of the as-prepared HB-Co_2P NCs.

The HER activity of the HB-Co_2P NCs in 0.5 M H_2SO_4 have been also evaluated. As shown in Fig. 4e, the HB-Co_2P NCs exhibit almost the same activity in acidic medium as in alkaline medium and demonstrate a low overpotential of ~107 mV at a current density of 10 mA cm^{-2} and ~128 mV for 20 mA cm^{-2}. Those values of η_{10} and η_{20} compare favorably to most of recently reported TMPs toward HER in acidic media (see Table 1). Tafel curve of the HB-Co_2P NCs gives a Tafel slope of 69 mV dec^{-1}, which was almost the same as this in alkaline media, indicating that the HB-Co_2P NCs have similar reaction kinetics in acidic and alkaline media. Directly comparison between the HB-Co_2P NCs and Co_2P nanorods[30] without splitting was made. The HB-Co_2P NCs in this work and the Co_2P nanorods reported by Huang[30] are both orthorhombic phase, and the mass loading for electrochemical performances tests are both 1 mg cm^{-2}. The Co_2P nanorods need overpotentials of 171 and 167 mV to achieve a current density of 20

Table 1 Summary of the HER performance of representative catalysts

Catalyst	Substrate	Mass loading (mg cm^{-2})	η_{10} (mV)	Tafel slope (mV dec^{-1})	Electrolyte
HB-Co_2P NCs in this work	Glassy carbon	1	100	67	1 M KOH
			107	69	0.5 M H_2SO_4
NiP_2 NSs/CC[31]	Carbon cloth	4.4	122	77	1 M KOH
NiP_2 NS/CC[42]	Carbon cloth	4.3	102	64	1 M KOH
NiP_2/CC[43]	Carbon cloth	3.8	158	93.4	1 M KOH
Ni_2P/Ni[44]	Ni foam		110	50	1 M KOH
NiCoP/rGO[45]	Glassy carbon	0.15	209	124.1	1 M KOH
Co_2P hollow NPs[11]	Ti foil	1	95	45	0.5 M H_2SO_4
Co_2P@NPG[27]	Glassy carbon	0.5	103	58	0.5 M H_2SO_4
			165	96	1 M KOH
Co_2P nanorod[30]	Ti foil	1	134	71	0.5 M H_2SO_4
CoP/BMHNC[33]	Glassy carbon	0.3	95.8	33	0.5 M H_2SO_4
Urchin-like CoP[32]	Glassy carbon	0.28	105	46	0.5 M H_2SO_4
CoP/CNT[46]	Glassy carbon	0.285	122	54	0.5 M H_2SO_4
MoP[20]	Glassy carbon	0.86	145	54	0.5 M H_2SO_4
			130	48	1 M KOH
CoP/CC nanowire arrays[18]	Carbon cloth	0.92	67	51	0.5 M H_2SO_4
			209	129	1 M KOH
FeP nanorod arrays[19]	Carbon cloth	1.5	58	45	0.5 M H_2SO_4
			218	146	1 M KOH
Ni_5P_4 [26]	Glassy carbon	1.99	118	42	0.5 M H_2SO_4
MoP[47]	Glassy carbon	0.36	125	54	0.5 M H_2SO_4
Co_2P nanowire[48]	—	—	~140	45	1 M KOH
CoP/rGO-400 [49]	Glassy carbon	0.28	105	50	0.5 M H_2SO_4
			150	38	1 M KOH
Mn–NiP_2 NSs/CC[31]	Carbon cloth	4.4	97	61	1 M KOH
Ni_2P/NF[50]	Ni foam	—	~150	93	1 M KOH

mA cm^{-2} in 1 M KOH and 0.5 M H_2SO_4 solution, respectively, and the overpotential increased by 12 mV after 1000 cycles in alkaline media. However, much smaller overpotentials were needed to achieve the same current density (121 and 128 mV in 1 M KOH and 0.5 M H_2SO_4 solution, respectively) for the HB-Co_2P NCs, and the overpotential increased by only 3 mV after 2000 cycles in alkaline media. The comparison suggests that the HB-Co_2P NCs show higher catalytic activities and better stability than the Co_2P nanorods without splitting.

So we can believe that the HB-Co_2P NCs might act as efficient HER electrocatalysts, and perform well in both of alkaline and acidic media. The high catalytic activity can be attributed to the following aspects: first, the unique charge natures of Co and P species, where the Co are positively charged and P are negatively charged, can facilitate the HER process. Second, the three-dimensional morphology gives the HB-Co_2P NCs a large specific surface area and provides more active sites for the catalytic reaction. What's more, the 3D structure has good structural stability and is not easy to agglomerate during the catalytic reaction, and can maintain high catalytic activity. Third, as mentioned, there are many kink sites in the individual nanofilaments,[41] indicating high density of crystal defects in the HB-Co_2P NCs. These crystal defects are usually highly active sites for the electrocatalytic reactions, and can greatly accelerate the HER process.

Conclusions

In summary, hyperbranched Co_2P nanocrystals with three-dimensional structure have been successfully prepared *via* a facile one-step synthetic strategy. The growth process of the HB-Co_2P NCs was revealed. At the initial stage of heat preservation (~1 min holding time), the crystal splitting occurs, and then the crystals grow up and the degree of crystal splitting increases with prolonging aging time. The obtained HB-Co_2P NCs exhibit high catalytic activities toward HER in both alkaline and acidic media. A large current density of 100 mA cm^{-2} can be achieved with a low overpotential of 185 and 189 mV in 1 M KOH and 0.5 M H_2SO_4, respectively. Long-term stability tests show that slight catalytic activity fading occurs after 2000 CV cycles or 22 h chronoamperometric testing in 1 M KOH. This facile method provides a possibility to produce low-cost metal phosphide electrocatalysts for hydrogen evolution in both alkaline and acidic media, which can cooperate with the OER catalysts to achieve the overall water splitting.

Conflicts of interest

There are no conflicts to declare.

Acknowledgements

This work was financially supported by the National Natural Science Foundation of China (Grant No. 51425401, 51690161, 51871045), Liaoning Innovative Research Team in University (Grant No. LT2017011), and the Fundamental Research Funds for the Central Universities (Grant No. N160907001, N180912004).

References

1 S. Carenco, D. Portehault, C. Boissiere, N. Mezailles and C. Sanchez, *Chem. Rev.*, 2013, **113**, 7981–8065.
2 J. Wang, F. Xu, H. Jin, Y. Chen and Y. Wang, *Adv. Mater.*, 2017, **29**, 1605838.
3 S. Anantharaj, S. R. Ede, K. Sakthikumar, K. Karthick, S. Mishra and S. Kundu, *ACS Catal.*, 2016, **6**, 8069–8097.
4 J. Wang, W. Cui, Q. Liu, Z. Xing, A. M. Asiri and X. Sun, *Adv. Mater.*, 2016, **28**, 215–230.
5 Y. Shi and B. Zhang, *Chem. Soc. Rev.*, 2016, **45**, 1529–1541.
6 J. Su, J. Zhou, L. Wang, C. Liu and Y. Chen, *Sci. Bull.*, 2017, **62**, 633–644.
7 P. Liu and J. A. Rodriguez, *J. Am. Chem. Soc.*, 2005, **127**, 14871–14878.
8 Y. Xu, R. Wu, J. Zhang, Y. Shi and B. Zhang, *Chem. Commun.*, 2013, **49**, 6656–6658.
9 Y. Shi, Y. Xu, S. Zhuo, J. Zhang and B. Zhang, *ACS Appl. Mater. Interfaces*, 2015, **7**, 2376–2384.
10 X. Yang, A.-Y. Lu, Y. Zhu, M. N. Hedhili, S. Min, K.-W. Huang, Y. Han and L.-J. Li, *Nano Energy*, 2015, **15**, 634–641.
11 J. F. Callejas, C. G. Read, E. J. Popczun, J. M. McEnaney and R. E. Schaak, *Chem. Mater.*, 2015, **27**, 3769–3774.
12 E. J. Popczun, C. G. Read, C. W. Roske, N. S. Lewis and R. E. Schaak, *Angew. Chem., Int. Ed.*, 2014, **53**, 5427–5430.
13 Y. Pan, Y. Liu, J. Zhao, K. Yang, J. Liang, D. Liu, W. Hu, D. Liu, Y. Liu and C. Liu, *J. Mater. Chem. A*, 2015, **3**, 1656–1665.
14 J. Wang, W. Yang and J. Liu, *J. Mater. Chem. A*, 2016, **4**, 4686–4690.
15 J. K. Kim, S.-K. Park and Y. C. Kang, *J. Alloys Compd.*, 2018, **763**, 652–661.
16 Z. Jin, P. Li and D. Xiao, *Green Chem.*, 2016, **18**, 1459–1464.
17 L. Yang, H. Qi, C. Zhang and X. Sun, *Nanotechnology*, 2016, **27**, 23LT01.
18 J. Tian, Q. Liu, A. M. Asiri and X. Sun, *J. Am. Chem. Soc.*, 2014, **136**, 7587–7590.
19 Y. Liang, Q. Liu, A. M. Asiri, X. Sun and Y. Luo, *ACS Catal.*, 2014, **4**, 4065–4069.
20 P. Xiao, M. A. Sk, L. Thia, X. Ge, R. J. Lim, J.-Y. Wang, K. H. Lim and X. Wang, *Energy Environ. Sci.*, 2014, **7**, 2624–2629.
21 D.-H. Ha, B. Han, M. Risch, L. Giordano, K. P. C. Yao, P. Karayaylali and Y. Shao-Horn, *Nano Energy*, 2016, **29**, 37–45.
22 J. Kibsgaard, C. Tsai, K. Chan, J. D. Benck, J. K. Nørskov, F. Abild-Pedersen and T. F. Jaramillo, *Energy Environ. Sci.*, 2015, **8**, 3022–3029.
23 T. Y. Ma, S. Dai, M. Jaroniec and S. Z. Qiao, *J. Am. Chem. Soc.*, 2014, **136**, 13925–13931.
24 X. Wang, W. Li, D. Xiong and L. Liu, *J. Mater. Chem. A*, 2016, **4**, 5639–5646.
25 R. Li, D. Zhou, J. Luo, W. Xu, J. Li, S. Li, P. Cheng and D. Yuan, *J. Power Sources*, 2017, **341**, 250–256.
26 A. B. Laursen, K. R. Patraju, M. J. Whitaker, M. Retuerto, T. Sarkar, N. Yao, K. V. Ramanujachary, M. Greenblatt and G. C. Dismukes, *Energy Environ. Sci.*, 2015, **8**, 1027–1034.
27 M. Zhuang, X. Ou, Y. Dou, L. Zhang, Q. Zhang, R. Wu, Y. Ding, M. Shao and Z. Luo, *Nano Lett.*, 2016, **16**, 4691–4698.
28 T. Liu, X. Ma, D. Liu, S. Hao, G. Du, Y. Ma, A. M. Asiri, X. Sun and L. Chen, *ACS Catal.*, 2016, **7**, 98–102.
29 J. F. Callejas, o. M. McEnaney, C. G. Read, J. C. Crompton, A. J. Biacchi, E. J. Popczun, T. R. Gordon, N. S. Lewis and A. R. E. Schaak, *ACS Nano*, 2014, **8**, 11101–11107.
30 Z. P. Huang, Z. Z. Chen, Z. B. Chen, C. C. Lv, M. G. Humphrey and C. Zhang, *Nano Energy*, 2014, **9**, 373–382.
31 X. Wang, H. Zhou, D. Zhang, M. Pi, J. Feng and S. Chen, *J. Power Sources*, 2018, **387**, 1–8.
32 H. Yang, Y. Zhang, F. Hu and Q. Wang, *Nano Lett.*, 2015, **15**, 7616–7620.
33 W. Yuan, X. Wang, X. Zhong and C. M. Li, *ACS Appl. Mater. Interfaces*, 2016, **8**, 20720–20729.
34 L. Xie, R. Zhang, L. Cui, D. Liu, S. Hao, Y. Ma, G. Du, A. M. Asiri and X. Sun, *Angew. Chem., Int. Ed.*, 2017, **56**, 1064–1068.
35 Y.-P. Zhu, Y.-P. Liu, T.-Z. Ren and Z.-Y. Yuan, *Adv. Funct. Mater.*, 2015, **25**, 7337–7347.
36 X. Wang, R. Tong, Y. Wang, H. Tao, Z. Zhang and H. Wang, *ACS Appl. Mater. Interfaces*, 2016, **8**, 34270–34279.
37 P. Quaino, F. Juarez, E. Santos and W. Schmickler, *Beilstein J. Nanotechnol.*, 2014, **5**, 846–854.
38 Y. Yan, B. Y. Xia, B. Zhao and X. Wang, *J. Mater. Chem. A*, 2016, **4**, 17587–17603.
39 J. Tang and A. P. Alivisatos, *Nano Lett.*, 2006, **6**, 2701–2706.
40 A. T. Kelly, I. Rusakova, T. Ould-Ely, C. Hofmann, A. Luttge and K. H. Whitmire, *Nano Lett.*, 2007, **7**, 2920–2925.
41 H. Zhang, D. H. Ha, R. Hovden, L. F. Kourkoutis and R. D. Robinson, *Nano Lett.*, 2011, **11**, 188–197.
42 P. Jiang, Q. Liu and X. Sun, *Nanoscale*, 2014, **6**, 13440–13445.
43 Z. Pu, Y. Xue, W. Li, I. S. Amiinu and S. Mu, *New J. Chem.*, 2017, **41**, 2154–2159.
44 Y. Shi, Y. Xu, S. Zhuo, J. Zhang and B. Zhang, *ACS Appl. Mater. Interfaces*, 2015, **7**, 2376–2384.
45 J. Li, M. Yan, X. Zhou, Z.-Q. Huang, Z. Xia, C.-R. Chang, Y. Ma and Y. Qu, *Adv. Funct. Mater.*, 2016, **26**, 6785–6796.
46 Q. Liu, J. Tian, W. Cui, P. Jiang, N. Cheng, A. M. Asiri and X. Sun, *Angew. Chem., Int. Ed.*, 2014, **53**, 6710–6714.
47 Z. Xing, Q. Liu, A. M. Asiri and X. Sun, *Adv. Mater.*, 2014, **26**, 5702–5707.
48 Z. Jin, P. Li and D. Xiao, *Green Chem.*, 2016, **18**, 1459–1464.
49 L. Jiao, Y.-X. Zhou and H.-L. Jiang, *Chem. Sci.*, 2016, **7**, 1690–1695.
50 B. You, N. Jiang, M. Sheng, M. W. Bhushan and Y. Sun, *ACS Catal.*, 2015, **6**, 714–721.
51 M. Gong, W. Zhou, M. C. Tsai, J. Zhou, M. Guan, M. C. Lin, B. Zhang, Y. Hu, D. Y. Wang, J. Yang, S. J. Pennycook, B. J. Hwang and H. Dai, *Nat. Commun.*, 2014, **5**, 4695.